JMEPEG (2016) 25:565–576
DOI: 10.1007/s11665-015-1815-4

1059-9495/$19.00

Effect of Welding Heat Input on the Corrosion Resistance of Carbon Steel Weld Metal

Yongxin Lu, Hongyang Jing, Yongdian Han, and Lianyong Xu

(Submitted August 28, 2015; in revised form November 14, 2015; published online December 21, 2015)

The corrosion resistance of carbon steel weld metal with three different microstructures has been systematically evaluated using electrochemical techniques with the simulated produced water containing CO_2 at 90 °C. Microstructures include acicular ferrite, polygonal ferrite, and a small amount of pearlite. With welding heat input increasing, weld metal microstructure becomes more uniform. Electrochemical techniques including potentiodynamic polarization curve, linear polarization resistance, and electrochemical impedance spectroscopy were utilized to characterize the corrosion properties on weld joint, indicating that the best corrosion resistance corresponded to the weld metal with a polygonal ferrite microstructure, whereas the weld metal with the acicular ferrite + polygonal ferrite microstructure showed the worst corrosion resistance. The samples with high welding heat input possessed better corrosion resistance. Results were discussed in terms of crystal plane orientation, grain size, and grain boundary type found in each weld metal by electron backscatter diffraction test.

Keywords corrosion, EBSD, EIS, steel, welding heat input

1. Introduction

Carbon dioxide (CO_2) corrosion, which easily gives rise to the failure of pipeline and equipment, is a common corrosion type in oil and gas industry (Ref 1, 2). This is generally because that crude oil and natural gas from the oil reservoirs/gas wells by pumping CO_2 with high pressures or CO_2 saturated water (CO_2-enhanced oil recovery technology) contain certain amount of CO_2 (Ref 1). And the presence of carbon dioxide in solution causes "sweet" corrosion due to the formation of a weak carbonic acid (H_2CO_3), which significantly drives CO_2 corrosion reactions (Ref 1, 3). However, CO_2-enhanced oil recovery technology has been widely applied in oil and gas industry field. Therefore, carbon steel corrosion in CO_2-containing solution is well known and studied (Ref 4–10).

Welding is the most common industrial method for connecting oil and gas pipes (Ref 11, 12). Nevertheless, it is hard to control the welding heat input during welding process (Ref 13). Welding heat input can be calculated by the following equation: heat input (KJ/mm) = voltage (V) × current (A)/travel speed (mm/s). It is well known that the greater the welding heat input, the slower the weld metal cooling rate (Ref 14). The cooling rate intensively influences weld metal microstructure (Ref 15), and then affects the local corrosion resistance of piping weld joint (Ref 12, 16, 17). Therefore, different cooling rates provide different microstructure and the corrosion resistance of weld metal changes with the variation of welding heat input.

During the welding thermal cycle, various types of ferrite are formed depending on factors such as the steel composition, heat input, cooling rate, and welding process (Ref 18, 19). The representatives are acicular ferrite (AF) and grain boundary ferrites (GBF), such as Widmanstatten and polygonal ferrite (PF) (Ref 12, 20). Whereas, the content of acicular ferrite and grain boundary ferrite in the weld metal often affects the corrosion resistance of weld metal (Ref 17). Deen et al. (Ref 16) researched the microstructure and electrochemical corrosion behavior of SA516 weld joint, and the result shows that the acicular ferrite structure provides lower corrosion resistance than allotriomorphic and widmanstatten ferrite. Huang et al. (Ref 17) studied that the influences of microstructure and composition on the electrochemical behavior of A516 steel weldment, and indicated that the electrochemical behavior of weld metal is dependent upon the volume fraction ratio of grain boundary ferrite to acicular ferrite. The number of acicular ferrite and grain boundary ferrite greatly depends on welding heat input. Hence, the corrosion performance of weld metal in the various environments is closely related to welding heat input. So, it is significant to determine the relationship between corrosion performance and welding heat input. However, the underlying effects of welding heat input on the corrosion resistance of carbon steel weld metal are still unclear.

Accordingly, in the present study, comparative studies of microstructural changes and corrosion resistance of carbon steel weld metal were conducted with different welding heat inputs. Particular emphasis was placed to understand the mechanism of corrosion resistance differences.

Yongxin Lu, Hongyang Jing, Yongdian Han, and **Lianyong Xu**, School of Materials Science and Engineering, Tianjin University, No. 92 Weijin Road, Tianjin 300072, People's Republic of China and Tianjin Key Laboratory of Advanced Joining Technology, Tianjin 300072, People's Republic of China. Contact e-mails: lyx2013@tju.edu.cn, hjing@tju.edu.cn, hanyongdian@tju.edu.cn, and xulianyong@tju.edu.cn.

2. Experiments

2.1 Welding Process

Two carbon steel (A106B) pipes, outer diameter of 219.1 mm and wall thickness of 10.3 mm, with V-grooves

Table 1 The weld parameters applied to obtain the welds

Parameters	W1		W2		W3	
	GTAW	SMAW	GTAW	SMAW	GTAW	SMAW
Heat input (KJ/mm)	0.83	1.54	1.30	1.76	1.80	1.93
Interpass temperature (°C)	33	80	35	87	39	95
Welding current (A)	106	140	127	184	180	145
Welding voltage (V)	9	22	10	14	14	20
Travel speed (mm/min)	69	120	59	88	84	90

Weld metal 1 = W1; weld metal 2 = W2; weld metal 3 = W3

Table 2 The chemical compositions of the A106B steel, ER70S-G filler, and weld metal

Composition (wt.%)	C	Mn	Si	S	P	Ni	Cr	Cu	Mo	Fe
A106B	0.21	0.42	0.28	0.01	0.02	0.012	0.023	< 0.01	< 0.01	Balance
ER70S-G	0.08	1.52	0.91	0.012	0.013	0.004	0.017	0.10	0.005	Balance
Weld metal	0.12	1.13	0.68	0.013	0.016	< 0.01	0.017	0.072	< 0.01	Balance

Table 3 Chemical composition (mg/L) of the corrosive solution

Ion category	Na^+	K^+	Ca^{2+}	Mg^{2+}	Fe^{2+}	Cl^-	SO_4^{2-}	HCO_3^-	CO_3^{2-}
Concentration (mg/L)	11193	548	1001	175.8	35.3	19747	603	245	0

were butt-welded with Gas Tungsten Arc Welding (GTAW) with ER70S-G filler. Each multipass weld was produced on prepared V-groove specimens with GTAW and Shielded Metal Arc Welding (GTAW + SMAW). Different welding heat input parameters, as shown in Table 1, were performed for obtaining the welds. The inner surface of the pipeline was exposed to a corrosive medium, so the following research focused on the root pass.

2.2 Material and Solution

The chemical compositions of the A106B steel, ER70S-G filler, and weld metal are shown in Table 2. The test samples (of $4 \times 8 \times 3$ mm dimensions) were cut from weld metal (WM). The samples were soldered to copper wires and then embedded in PVC holder with epoxy resin. Prior to test, the specimens were ground up to 1000 grit silicon carbide paper, rinsed with deionized water, and degreased in acetone. Test solution was composed of analytical grade reagents and deionized water, simulating the produced water drawn out from oil and gas fields. Its chemical composition is listed in Table 3. The corrosive solution was deoxygenated by bubbling pure N_2 through it for 12 h before introducing the CO_2. The temperature of the test was 90 °C, the CO_2 partial pressure of 0.02 MPa, the whole pressure of 0.3 MPa, and the pH of the test solution ranged from 4.3 to 4.6.

2.3 Electrochemical Experiments

The linear polarization resistance (LPR), potentiodynamic polarization, and electrochemical impedance spectroscopy (EIS) tests were performed by using an electrochemical workstation (Gamry Interface 1000) and a 10 L high temperature and high pressure autoclave. A platinum sheet was

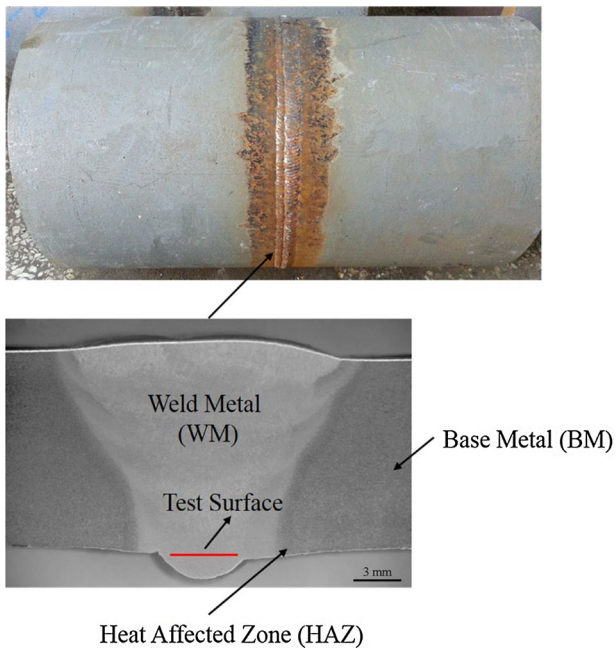

Fig. 1 The schematic of test position in the weld joint

counter electrode (CE), and an Ag/AgCl probe (1 mol/L KCl) with high temperature/pressure was reference electrode (RE). The samples were the working electrode (WE). Polarization curves were recorded at a constant sweep rate of 0.5 mV/s at a −0.3 to +0.3 V interval respect to open circuit potential (OCP). Corrosion current density (i_{corr}) was calculated by using the Tafel extrapolation method and taking an extrapolation interval

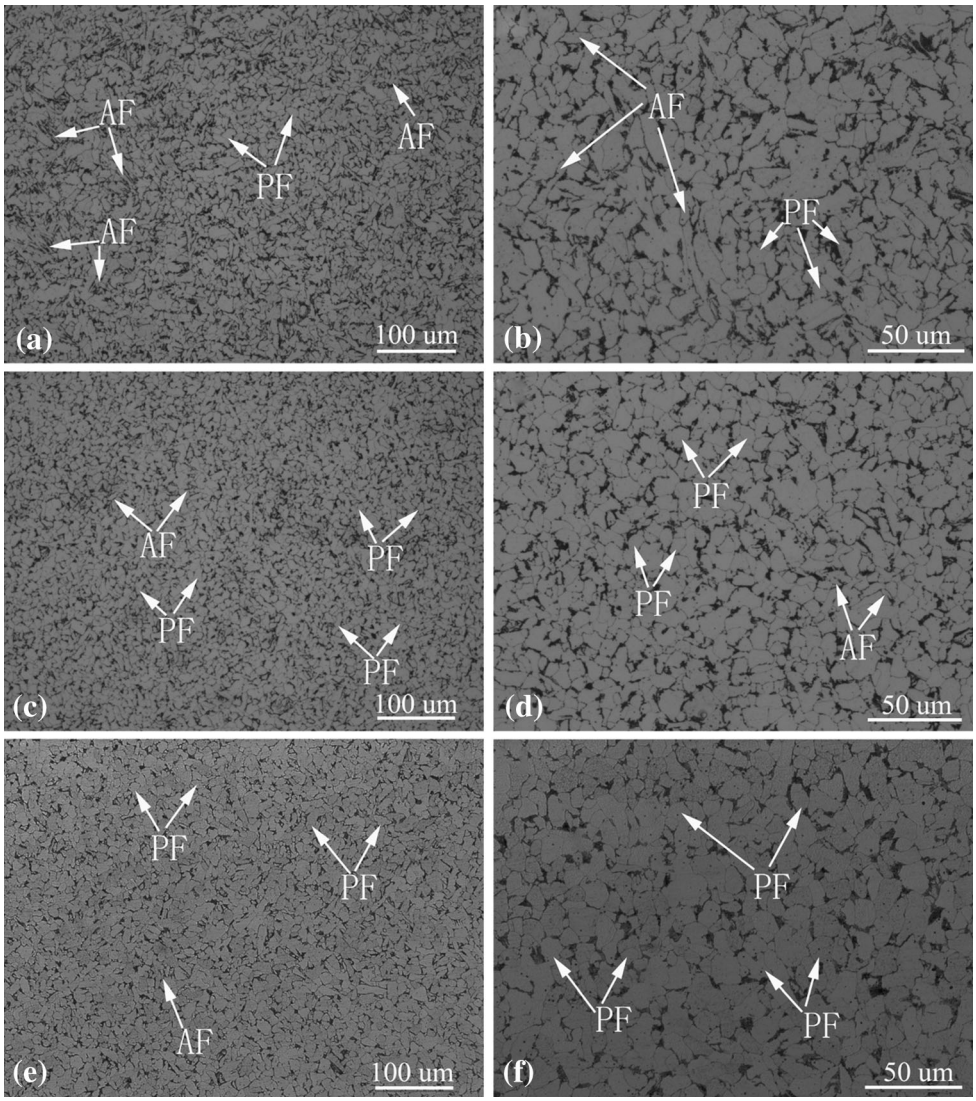

Fig. 2 The microstructure at the bottom center of different welding heat input samples (a and b: W1; c and d: W2; e and f: W3)

of ±250 mV around the stable E_{corr}. LPR tests were carried out by polarizing the specimen from +10 to −10 mV in respect to OCP at a scanning rate of 0.125 mV/s during 36 h. Electrochemical impedance spectroscopy (EIS) tests were carried out at OCP by using a signal with the amplitude of 5 mV in a frequency range from 100 KHz to 10 mHz. The Kramers-Kronig transforms was used to validate the electrochemical impedance data, and the ZSimpWin V3.10 impedance analysis software was used to fit the achieved data.

2.4 EBSD Tests

The corroded sample surface was defined as the normal direction (ND). The gage length and width of the drawing sample were parallel to the drawing direction (RD) and traverse direction (TD) of the cold-drawing, respectively. Three specimens (of 12 × 8 × 6 mm dimensions) with different welding heat inputs were sectioned to three equal parts from the drawing direction. Then, the bottom of specimens was polished with an

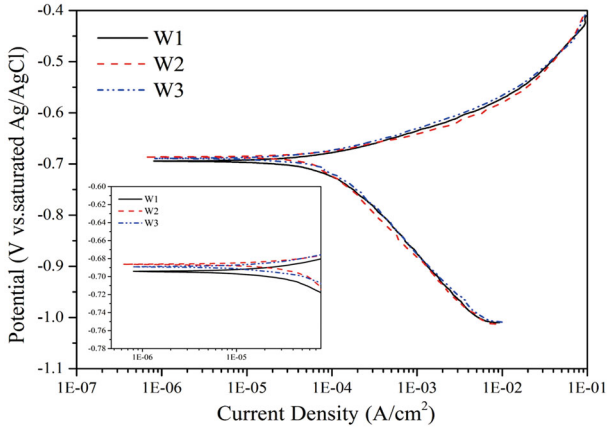

Fig. 3 Comparison of experimental potentiodynamic polarization curves of samples

Table 4 Potentiodynamic polarization curve parameters

Sample	E_{corr}(mV vs. Ag/AgCl)	I_{corr}(μA/cm^2)	β_a(mV/decade)	β_c(mV/decade)	$CR_{(Tafel)}$(mmpy)
W1	−694.0	182.0	79.50	−215.20	2.115
W2	−686.0	134.0	76.70	−214.20	1.531
W3	−689.0	111.0	66.60	−196.60	1.294

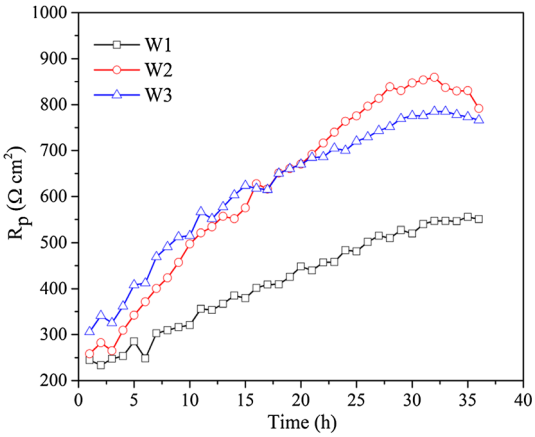

Fig. 4 The dependence of the linear polarization resistance (R_p) on the time

electrolyte solution that consisted of 650 mL of alcohol, 100 mL of perchloric acid, and 50 mL of distilled water (General Research Institute for Nonferrous Metals, Beijing, China) at 30 V for 10 s at 20 °C (Ref 21). After polishing, three specimens were investigated with a JEOL JSM-7001F scanning electron microscope with an Oxford Instruments Nordlys nano EBSD detector. All tests were done at the bottom center of specimens. When EBSD tests were completed, EBSD original data were analyzed by using TSL OIM 6 Analysis software.

3. Results and Discussion

3.1 Microstructural Observation

The samples were cut from a whole pipeline, and the test surface is shown in Fig. 1. The microstructure at the bottom center of samples with different welding heat inputs was observed by using Leica DMI5000M. As it can be seen from Fig. 2, the microstructure mainly contained pearlite (dark areas) and ferrite (white areas). The representative acicular ferrite (AF) and polygonal ferrite (PF) were distinguished according to the International Institute of Welding (IIW) microstructure classification scheme for ferrous weld metals (Ref 18, 22). Ferrite phases were found as acicular ferrite (AF) and irregular polygonal ferrite (PF), and grain boundaries were clear. The number of acicular ferrite decreased and the number of irregular polygonal ferrite increased with welding heat input increasing. Pearlite phase was found as irregular polygonal shape. Generally, polygonal ferrite firstly nucleated at austenite grain boundary, lengthened along the boundary, and thickened into the grain to form the equiaxed or near-equiaxed ferrite grains (Ref 23). The number of irregular polygonal ferrite increasing was caused by the large heat input and subsequent weld heat treatment. The recrystallization happened and a large number of irregular polygonal ferrite grains would form. Therefore, the weld metal microstructure became more uniform with welding heat input increasing.

3.2 Potentiodynamic Polarization and Linear Polarization Resistance Tests

A comparison of experimental potentiodynamic polarization curves for different samples in simulated produced water containing CO_2 is shown in Fig. 3. It was found that three samples of active dissolution occurred during the anodic polarization process from Fig. 3. Using both the cathodic and anodic branches of these polarization curves between −250 mV (Ag/AgCl) and +250 mV (Ag/AgCl) around the stable E_{corr}, the polarization curve parameters were obtained through Tafel's extrapolation by using the Gamry Echem analysis software, as shown in Table 4, indicating E_{corr} for weld metals were very similar and the active values happened around −685 mV (Ag/AgCl). The maximum current density (i_{corr}) was for weld metal W1 (around 182 μA/cm^2), while the minimum current density was for weld metal W3 (around 111 μA/cm^2). It is apparent to see that current density decreased with welding heat input increasing.

Electrochemical corrosion monitoring using the linear polarization resistance (LPR) method is well established for the determination of average corrosion rate, and the method is relatively simple to implement (Ref 24, 25). The dependence of the linear polarization resistance (R_p) on the time (Ref 26, 27) is displayed in Fig. 4. It can be seen that the minimum R_p, and thus the maximum i_{corr} was for weld metal W1, whereas the R_p for weld metal W2 and W3 was the almost same, and the R_p for the weld metal W2 exceeded that for weld metal W3 around 18 h. The R_p increased with the time, indicating a decrease in the corrosion rate as time elapsed. This behavior can be attributed to the fact that at the start of the test, the surface of the specimens was clean and consequently active. After a period of time, the corrosion product film formed on the sample surface, isolating the metal from the environment and decreasing the corrosion rate (Ref 11). According some researchers, the initial product film formed in the corrosion of the steel in "sweet" environment is $FeCO_3$ mainly (Ref 3, 28, 29).

3.3 Electrochemical Impedance Spectroscopy (EIS) Tests

Electrochemical impedance spectroscopy tests were carried out at OCP for different samples. In order to validate the results of EIS and check the system whether to meet the constraints of Linear System Theory (LST) and three basic prerequisites (causality, linearity, and stability) (Ref 30). The K-K transforms had been applied to the EIS measurements by transforming the real axis into the imaginary axis and the imaginary axis into the real axis (Ref 31–33). Figure 5 shows the similar results between the experiment points and corresponding K-K transforms, confirming that the system satisfies the constraints of

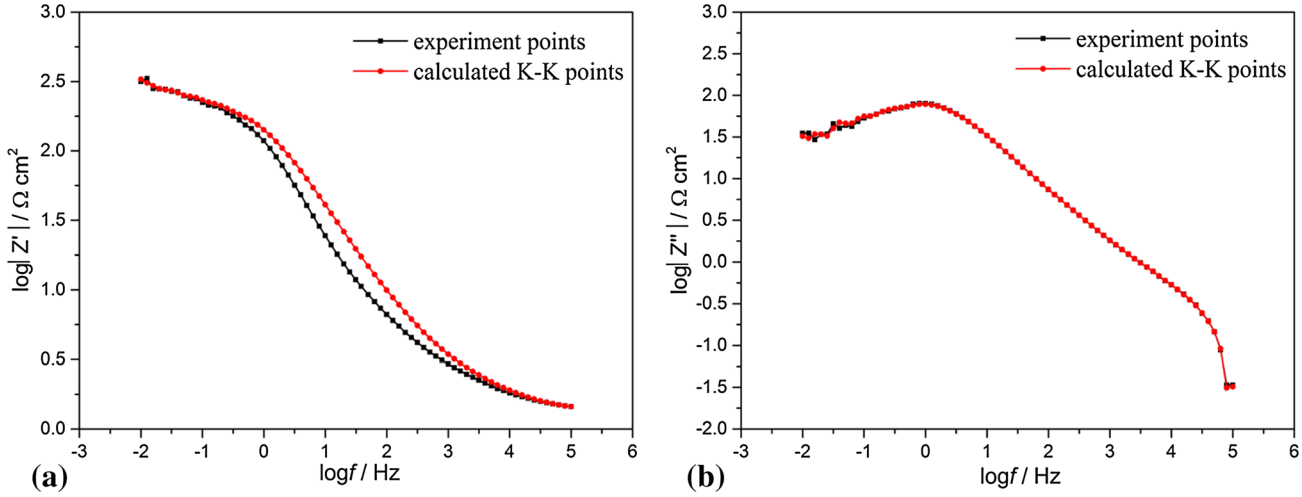

Fig. 5 K-K transforms of EIS data for weld metal W2 at 10 h in CO_2-containing simulated produced water

Table 5 Parameters used to simulate the EIS data for weld metal W3

	Time (h)								
Elements	**2**	**6**	**10**	**12**	**18**	**24**	**30**	**32**	**36**
R_s (Ω)	0.5345	0.5590	0.5654	0.5669	0.5768	0.5745	0.5781	0.5790	0.5788
Q_f (Ss^n/cm^{-2})	3.56×10^{-03}	3.25×10^{-03}	3.41×10^{-03}	3.43×10^{-03}	3.67×10^{-03}	3.75×10^{-03}	3.72×10^{-03}	3.69×10^{-03}	3.64×10^{-03}
n ($0 < n < 1$)	0.6301	0.6695	0.6730	0.6776	0.6812	0.6813	0.6805	0.6810	0.6806
R_{pore} (Ω cm^2)	3.447	18.78	20.63	20.22	21.13	13.46	15.26	16.23	17.43
Q_{dl} (Ss^n/cm^2)	3.18×10^{-04}	1.37×10^{-04}	1.25×10^{-04}	1.28×10^{-04}	1.17×10^{-04}	1.18×10^{-04}	1.31×10^{-04}	1.37×10^{-04}	1.68×10^{-04}
n ($0 < n < 1$)	0.8936	1	1	1	1	1	1	1	1
R_{ct} (Ω cm^2)	80.26	111.8	149.7	159.6	186.4	206.5	211.1	209.0	195.3
χ^2	7.79×10^{-03}	1.35×10^{-03}	6.61×10^{-04}	6.12×10^{-04}	9.90×10^{-04}	1.90×10^{-04}	2.12×10^{-03}	1.97×10^{-03}	1.76×10^{-03}

Linear System Theory (Ref 31–34). Therefore, the EIS results of present study were valid.

The electrochemical impedance spectroscopy test results in the Nyquist format for three weld metals during 36 h are shown in Fig. 6. As it can be seen from Fig. 6, the spectra were characterized by two time constants: a high frequency capacitive loop associated with the charge transfer process occurring at the steel-electrolyte interface, and a low-frequency capacitive loop related to the adsorbed intermediate product and the amorphous film formed during the dissolution of electrode (Ref 7, 35). In previous works, at the initial immersion stage (about 0-7 h), the EIS character was attributed to the increased surface area between the substrate and electrolyte which was beneficial to the cathodic reaction and galvanic corrosion effect, indicating that a corrosion process was controlled by charge transfer (Ref 36). For immersion time longer than 7 h, the EIS character could be owed to the porous corrosion scale, manifesting the corrosion mechanism changed from electrochemical steps control to mixed control of mass transfer and charge transfer (Ref 36). In the study, the turning point of EIS character was 10 h, as shown in Fig. 6. Within 10 hours, the semicircle diameter of weld metal W1 was less than those of weld metal W2 and W3 in the Nyquist, so there was more surface area in weld metal W1, which was beneficial for the cathodic reaction and galvanic corrosion effect. After 10 hours, the semicircle diameter of weld metal W1 was less than those of weld metal W2 and W3 in the Nyquist, hence there were more holes in the corrosion scale of weld metal W1, and those holes were conductive to mass transfer and charge transfer. In a word, the smallest semicircle diameter was monitored in the weld metal W1, while the largest semicircle diameter was observed in the weld metal W2, indicating that the corrosion impedance increased at first and then decreased slightly with welding heat input increasing.

Schematic representation of the interfacial reactions and equivalent electrical circuit used to simulate EIS data is shown in Fig. 7. The impedance parameters were determined by using this equivalent circuit and the ZSimpWin V3.10 impedance analysis software. In the equivalent electrical circuit, R_s is the solution resistance, Q_f is the constant phase element (CPE) which represents the capacitance of porous corrosion scale, R_{pore} is the resistance of porous corrosion scale, Q_{dl} is the constant phase element (CPE) which represents the capacitance of double layer, and R_{ct} is the charge transfer resistance. The constant phase element (CPE) is used instead of a capacitance to take the non-ideal interface behavior into account. The CPE is given by

$$Z_{CPE} = (1/Y_0)(jw)^{-n}, \quad \text{(Eq 1)}$$

where Y_0 is a proportional factor, $j = \sqrt{-1}$, $w = 2\pi f$, n is the dispersion coefficient related to surface inhomogeneity. For $n = 0$, it represents a resistance with $R = Y_0^{-1}$; for $n = 1$, it represents a capacitance with $C = Y_0$. For example, the parameters which were calculated for simulating EIS data of

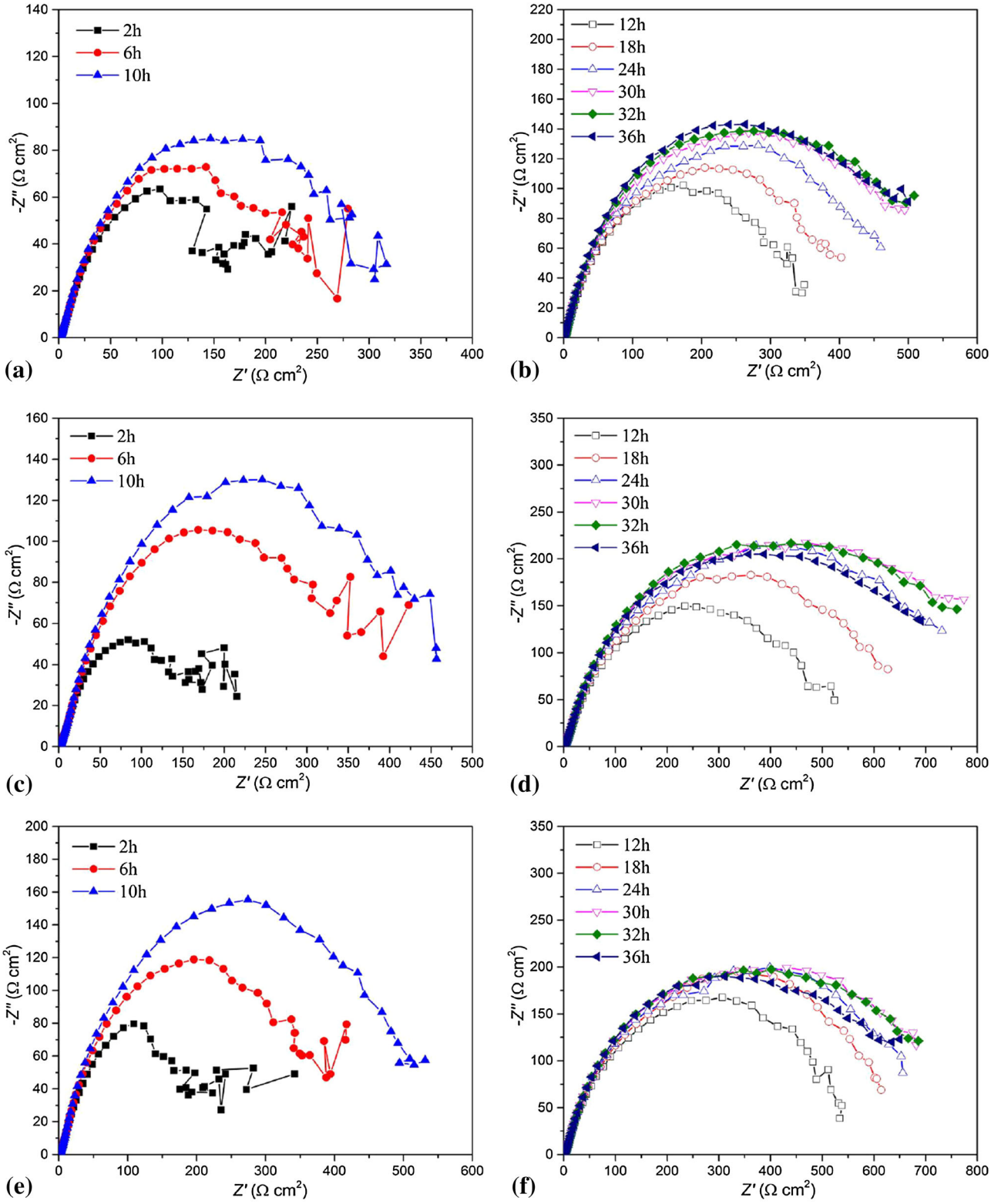

Fig. 6 Nyquist diagram for weld metal in CO_2-containing simulated produced water (a and b: W1, c and d: W2, e and f: W3)

weld metal W3 by using the circuits shown in Fig. 7(b) are listed in Table 5. The agreement between the experimental and simulated values was demonstrated by the chi-squared values between 1.90×10^{-4} and 7.79×10^{-3}, indicating a good fitting quality.

The R_{ct} and R_{pore} calculated from the experimental data in Fig. 6 are shown in Fig. 8 and 9, respectively. It can be seen from Fig. 8 that R_{ct} of weld metal W2 was close to that of weld metal W3, and they were higher than R_{ct} of weld metal W1. The R_{ct} increased with time, and then kept a stable value at

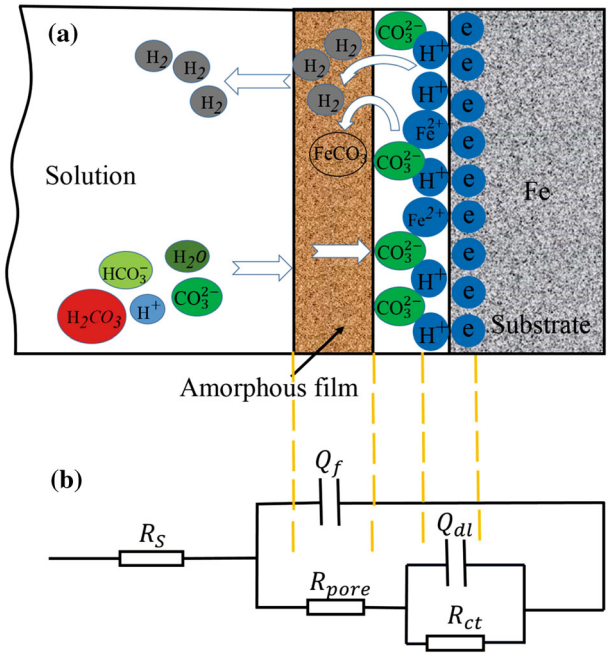

Fig. 7 Schematic representation of the interfacial reactions (a) and equivalent electrical circuit used to simulate EIS data (b)

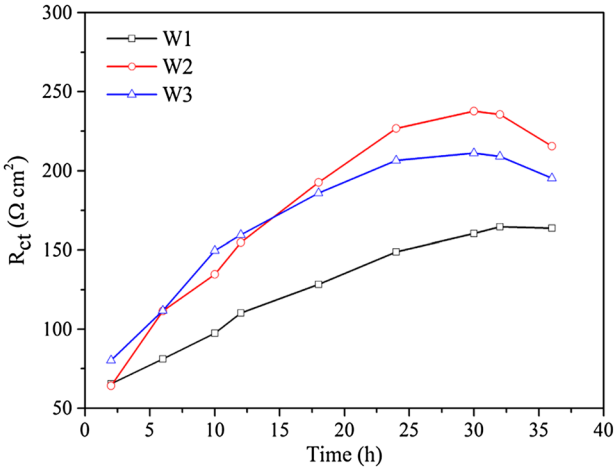

Fig. 8 Change in the calculated charge transfer resistance R_{ct} with time for weld metal W1, W2, and W3

around 30 h. The variation of R_{ct} was due to the change of electrode surface state with the immersion time. Because the corrosion rate was inversely proportional to R_{ct} (Ref 36), i.e., the corrosion rate reached a stable value after 30 h immersion.

It can be seen from Fig. 9 that R_{pore} increased quickly at initial immersion time (before 6 h), then kept a stable value with longer immersion time. The corrosion scale resistance was small, showing the corrosion scale was porous and loose (Ref 27). From Fig. 8 and 9, it can be seen that R_{ct} values were much higher than R_{pore} values, indicating that the reason of the increase in the total impedance was the sample surface active state, thus demonstrating the surface activity of W1 was more intensity.

As discussed in previous works (Ref 36), the interfacial dissolution processes of Fe in CO_2-saturated solution were divided into two different states: charge transfer control, and

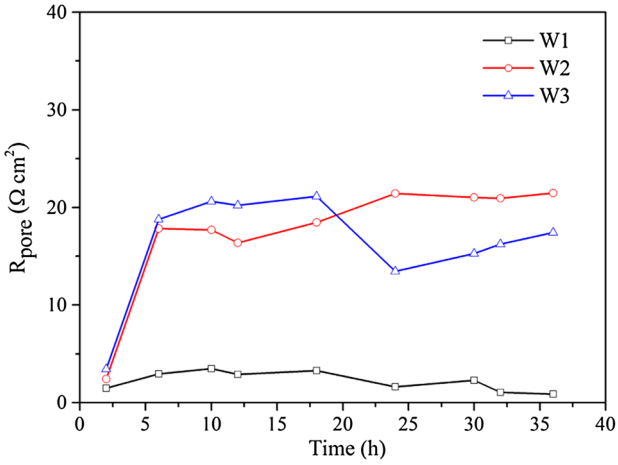

Fig. 9 Change in the calculated corrosion scale resistance R_{pore} with time for weld metal W1, W2, and W3

mixed control of mass transfer and charge transfer. The processes follow the consecutive steps (Ref 7, 37, 38):

$$\underset{1-\theta_1}{\mathrm{Fe}} + \mathrm{H_2O} \overset{k_1}{\underset{k_{-1}}{}} \underset{\theta_1}{\mathrm{Fe(OH)_{ads}}} + \mathrm{H^+} + \mathrm{e} \quad \text{(Eq 2)}$$

$$\underset{\theta_1}{\mathrm{Fe(OH)_{ads}}} \xrightarrow{K_2} \mathrm{FeOH^+} + \mathrm{e} \quad \text{(Eq 3)}$$

$$\mathrm{FeOH^+} + \mathrm{H^+} = \mathrm{Fe^{2+}} + \mathrm{H_2O} \quad \text{(Eq 4)}$$

$$\underset{1-\theta_1-\theta_2}{\mathrm{Fe}} + \mathrm{HCO_3^-} \xrightarrow{K_3} \underset{\theta_2}{\mathrm{FeCO_3}} + \mathrm{H^+} + 2\mathrm{e} \quad \text{(Eq 5)}$$

$$\mathrm{FeCO_3} + \mathrm{HCO_3^-} \xrightarrow{K_4} \mathrm{Fe(CO_3)_2^{2-}} + \mathrm{H^+}, \quad \text{(Eq 6)}$$

where θ_1 and θ_2 are the coverage of intermediate adsorbed product $Fe(OH)_{ads}$ and corrosion product $FeCO_3$. K_{+1}, K_{-1}, K_2, K_3 and K_4 are the reaction rate constants (Ref 7, 39). The dissolution of Fe and the formation of corrosion scale happen on the surface without the intermediate adsorbed product and corrosion product. Therefore, the reaction current density can be expressed as $I_{+1} = k_{+1}(1 - \theta_1 - \theta_2)$; $I_{-1} = k_{-1}C_{H^+}\theta_1$; $I_1 = I_{+1} - I_{-1}$; $I_2 = k_2\theta_1$; $I_3 = k_3 C_{HCO_3^-}(1 - \theta_1 - \theta_2)$; $I_4 = k_4 C_{HCO_3^-}\theta_2$, where I_{+1} and I_{-1} are the forward and afterward reaction current densities, respectively. So, the whole current density of active region can be expressed as follows:

$$I_a = I_1 + I_3. \quad \text{(Eq 7)}$$

The whole current density of the intermediate adsorbed product and corrosion product can be expressed as follows:

$$I_f = I_2 + I_4 \quad \text{(Eq 8)}$$

Accordingly, the faradic current density of anodic reaction can be expressed as follows:

$$I_F = I_a + I_f. \quad \text{(Eq 9)}$$

The electrode process was affected by θ_1 and θ_2 besides electrode potential E, and then the increase rate of θ_1 and θ_2 can be expressed as follows: $\theta_1' = d\theta_1/dt = K_1(I_1 - I_2)$; $\theta_2' = d\theta_2/dt = K_2(I_3 - I_4)$, where K_1 and K_2 are the coverage-electricity conversion coefficients, respectively.

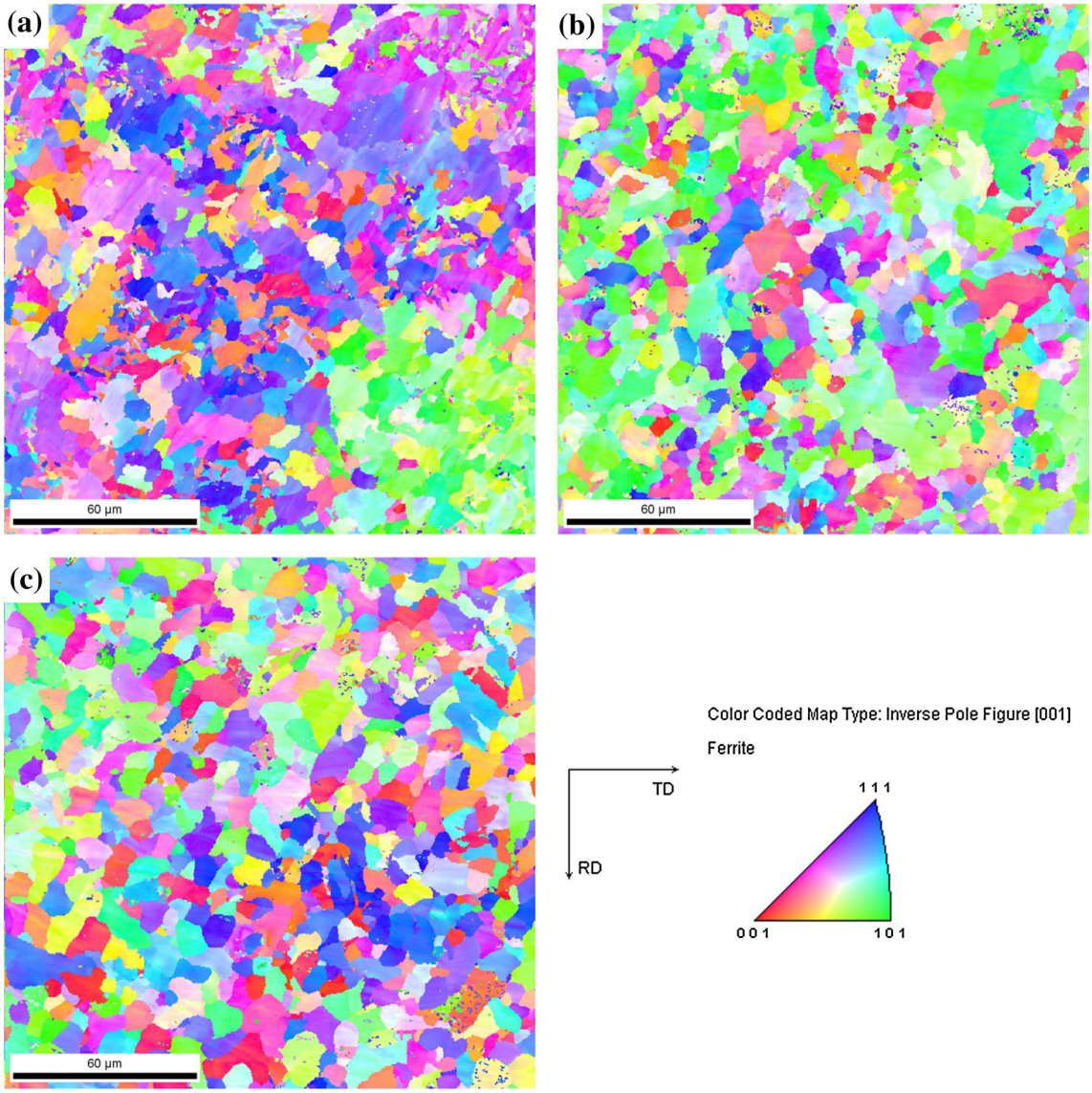

Fig. 10 IPF color map at the bottom center of samples ((a) W1, (b) W2, and (c) W3. For interpretation of the references to color in this figure legend, the reader is referred to the web version of this article)

Cao (Ref 40) believed that if the electrode reaction was controlled by two-surface state variable X_1 and X_2, then the faradic admittance Y_F could be described as

$$Y_F = 1/R_t + (A + j\omega B)/(D - \omega_2 + j\omega T), \quad \text{(Eq 10)}$$

where $1/R_t = (\partial I_F/\partial E)_{SS}$; $A = m_1 b_2 J_{12} + m_2 b_1 J_{21} - m_1 b_1 J_{22} - m_2 b_2 J_{11}$; $B = m_1 b_1 + m_2 b_2$; $D = J_{11} J_{22} - J_{12} J_{21}$; $T = -(J_{11} + J_{22})$.

The variables of m_1, b_1, m_2, b_2, J_{11}, J_{12}, J_{21}, and J_{22} can be calculated by the following equations:

$$m_1 = (\partial I_F/\partial \theta_1)_{SS} = (\partial I_a/\partial \theta_1)_{SS} + (\partial I_f/\partial \theta_1)_{SS} = -k_1 - k_{-1} C_{H^+} + k_2 - k_3 C_{HCO_3^-}; \quad \text{(Eq 11)}$$

$$m_2 = (\partial I_F/\partial \theta_2)_{SS} = (\partial I_a/\partial \theta_2)_{SS} + (\partial I_f/\partial \theta_2)_{SS} = -k_1 - k_3 C_{HCO_3^-}; \quad \text{(Eq 12)}$$

$$b_1 = (\partial \theta_1'/dE)_{SS} = K_1 (\partial I_1/\partial E - \partial I_2/\partial E)_{SS}; \quad \text{(Eq 13)}$$

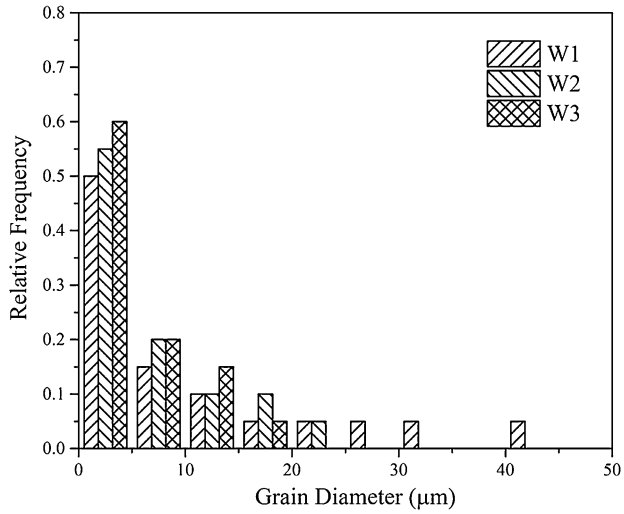

Fig. 11 The relative frequency of grain size distribution at the bottom center of samples

$$b_2 = \left(\partial\theta_2'/dE\right)_{SS} = K_2(\partial I_3/\partial E - \partial I_4/\partial E)_{SS}; \quad \text{(Eq 14)}$$

$$J_{11} = \left(\partial\theta_1'/d\theta_1\right)_{SS} = -K_1(k_1 + k_{-1}C_{H^+} + k_2)_{SS}; \quad \text{(Eq 15)}$$

$$J_{12} = \left(\partial\theta_1'/d\theta_2\right)_{SS} = -K_1k_1; \quad \text{(Eq 16)}$$

$$J_{21} = \left(\partial\theta_2'/d\theta_1\right)_{SS} = -K_2k_3C_{HCO_3^-}; \quad \text{(Eq 17)}$$

$$J_{22} = \left(\partial\theta_2'/d\theta_2\right)_{SS} = -K_2\left(k_3C_{HCO_3^-} + k_4C_{HCO_3^-}\right), \quad \text{(Eq 18)}$$

where the subscript 'SS' denotes steady state. It is obviously that $A > 0$and $B = m_1b_1 + m_2b_2 = (K_1F/RT)[(1-\alpha_1)I_{+1} + \alpha_1I_{-1}]\left(-k_1 - k_{-1}C_{H^+} + k_2 - k_3C_{HCO_3^-}\right)$. It is well known that equation (3) is the reaction control step and the k_2 value is vey small, so B <0. According to the theory of Cao (Ref 40), when $A > 0$ and $B < 0$, the impedance plane would exhibit a capacitive loop at low-frequency position. The above theoretical calculation is in agreement with the experiment results shown in Fig. 6.

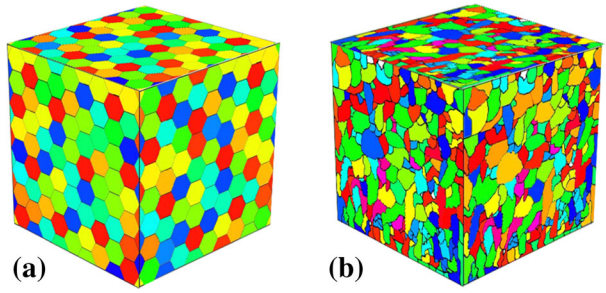

Fig. 12 Simulated grain structures illustrating an (a) ideal and (b) random structure with α values of approximately 1 and 0.5, respectively

3.4 EBSD Tests

The primary objective of EBSD tests carried out in this study was to determine the distribution of grain size, crystal plane orientation, and grain boundary type of the test samples. Figure 10(a)–(c) shows the inverse pole figure (IPF) map at the bottom center of different welding heat input specimens. The region always touched the corrosion medium when the weld was in service. Therefore, IPF maps were constructed in the region in all specimens. IPF maps, as shown in Fig. 10(a)–(c), show an accumulation of grain with ⟨111⟩⊥ND orientation in weld metal W1 surface, while ⟨101⟩⊥ND orientation in weld

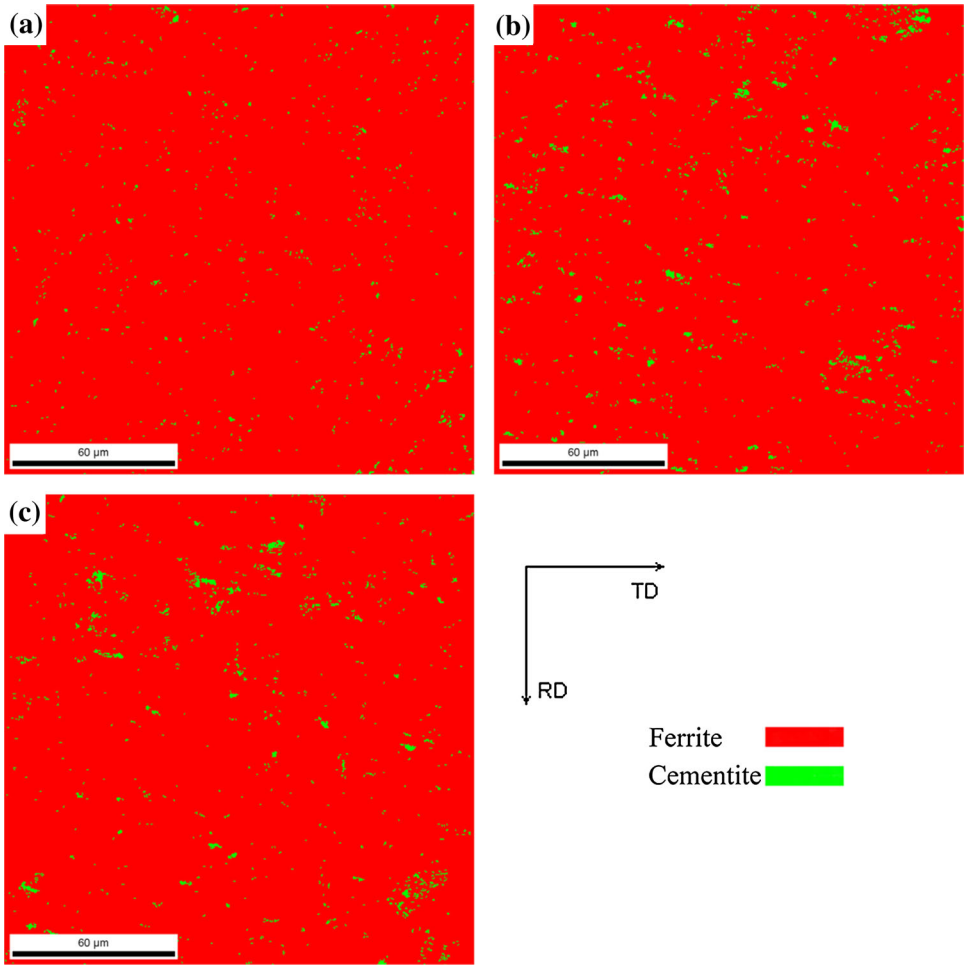

Fig. 13 The distribution of ferrite and cementite at the bottom center of samples ((a) W1, (b) W2, and (c) W3. For interpretation of the references to color in this figure legend, the reader is referred to the web version of this article)

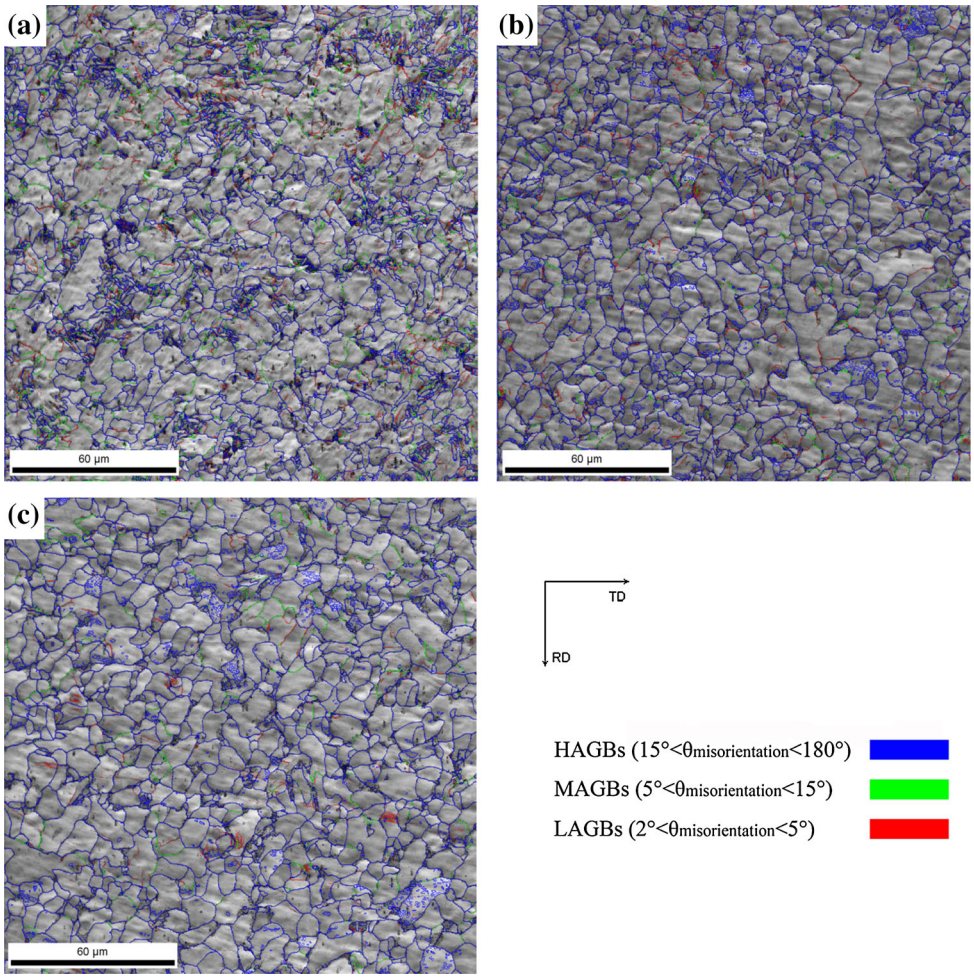

Fig. 14 EBSD reconstructed grain boundary map at the bottom center of samples ((a) W1, (b) W2, and (c) W3. For interpretation of the references to color in this figure legend, the reader is referred to the web version of this article)

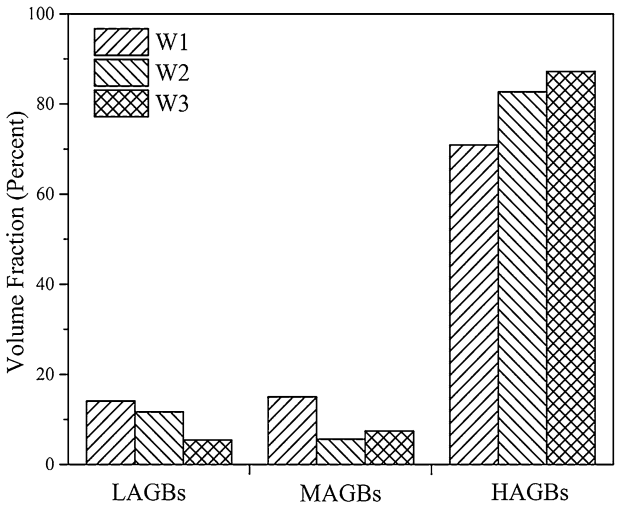

Fig. 15 Volume fraction of LABs, MABs, and HABs at the bottom center of samples

metal W2 and W3 surface. In other words, there were more grains with ⟨111⟩⊥ND orientation in weld metal W1 surface, and more grains with ⟨101⟩⊥ND orientation in weld metal W2 and W3 surface. The electrochemical test results showed the corrosion resistance of weld metal W2 and W3 was superior to weld metal W1. According to the broken bond theory, the surface free energy of crystal planes {h k l} for BCC metal is approximately equal to $6hE_b/4d^2\sqrt{h^2+k^2+l^2}$ or $3E_b(h+k+l)/4d^2\sqrt{h^2+k^2+l^2}$ (Ref 41), "E_b" is the bond energy identified as the enthalpy changes during the sublimation process (Ref 42); and "d" is the bond length between two nearest neighbor atoms. Calculated the surface free energy, {101} was the crystal face with the lowest energy, and the ranking of surface free energy should be $\{101\} < \{111\} < \{001\}$. The {101} with the lowest energy dissolved slower than the crystal face of other orientations, which was consistent with our current observation. The result was attributed to the atoms in the lower surface energy planes were the most difficult to dissolve (Ref 43). At the same time, corrosion, as a surface-dependent property, was an anisotropic characteristic of materials (Ref 44, 45). It was observed that the corrosion rate anisotropy corresponded with surface energy anisotropy in this study.

The grain size distribution at the bottom center of weld metal W1, W2, and W3 is shown in Fig. 11. As shown in this figure, the relative frequency of fine grains (less than 10 μm in diameter) in weld metal W2 and W3 is higher than that in weld

metal W1. The average grain size is 10.2702 ± 2.5967 μm (W1), 6.6349 ± 1.4956 μm (W2), and 5.3344 ± 1.1236 μm (W3), respectively. It shows that microstructures become more uniform with welding heat input increasing. Meanwhile, the maximum grain size of W2 and W3 is around 20 μm, while the maximum grain size of W1 is around 40 μm. Based on the hypothesis of grain boundary conduction and reactivity, i_{corr} should vary with grain boundary length. Ralston et al. (Ref 46) proposed that the grain boundary length (*gbl*) can be presented as

$$gbl = (C) + (D)gs^{-\alpha}, \quad 0.5 \leq \alpha \leq 1, \qquad \text{(Eq 19)}$$

where the constant C is an area term and D is a scale term, and gs is the grain size. In the ideal case, for perfectly equiaxed grains, $\alpha = 1$ (as shown in Fig. 12a), while for the random grain structures with dispersed relationships, $\alpha = 0.5$ (as shown in Fig. 12b). Assume that the constants C and D are invariant for weld metals. According to the equation (19), the ranking of grain boundary length (*gbl*) should be W1 (C+0.40D) > W2 (C+0.28D) > W3 (C+0.22D). Under a non-passivating condition, grain boundary densities would enhance overall surface reactivity. Therefore, i_{corr} increased with grain boundary length increasing, i.e., i_{corr} of weld metal W1 was higher than that of weld metal W2 and W3.

The distribution of ferrite and cementite at the bottom center of weld metal W1, W2, and W3 is shown in Fig. 13. Ferrite and cementite are shown with red and green colors, respectively. The volume fractions of cementite at the bottom center of three specimens were 1.0, 2.1, and 1.6 % for W1, W2, and W3, respectively. It was found a ruleless volume fraction of ferrite and cementite with the change of welding heat input. Hunnik et al. (Ref 47) reported that the effect of cathodic regions of the cementite was considerable in carbon steels with carbon content higher than approximately 0.15 wt.%. In this work, the weld metal used for electrochemical tests had a carbon content of 0.12 wt.%, as shown in Table 2. It can deduce that the galvanic effect of cementite in weld metal was not the main reason for the difference in corrosion rate observed as shown in Fig. 3.

Figure 14 shows the distribution of high-angle grain boundaries (HAGBs), medium-angle grain boundaries (MAGBs), and low-angle grain boundaries (LAGBs) in weld metals. A grain boundary with a misorientation angle of $15° < \theta < 180°$, $5° < \theta < 15°$, and $2° < \theta < 5°$ was considered as a HAGB, MAGB, and LAGB, respectively. In Fig. 14, HAGB, MAGB, and LAGB are shown with black, blue, and green lines colors, respectively. As shown in Fig. 14(a)–(c), the number of HAGBs becomes more and more with welding heat input increasing. The accumulation indicates that the recrystallization process completed in these regions with welding heat input increasing. The volume fraction of three type grain boundaries is shown in Fig. 15. It was shown that the volume fraction of LAGBs and MAGB was highest in the weld metal W1. And a high volume fraction of HAGBs in weld metal W3 indicated that a high amount of LAGBs had been changed to HAGBs during recrystallization and therefore the volume fraction of LAGBs decreased. It was commonly believed that the energy of HAGBs was higher than that of LAGBs due to the high level of the atomic non-coherent arrangement. Therefore, high-angle grain boundaries (HAGBs) were more vulnerable to local corrosion along grain boundaries than low-angle grain boundaries (LAGBs) (Ref 48, 49). It should be noted that the number of HAGBs for samples in Fig. 15 increased in the following order: W1 < W2 < W3. Thus, combined with the grain orientation and grain size analysis, the effect of grain boundaries was inferior to that of the grain orientation and grain size on the corrosion resistance of A106B steel weld metal in CO_2-containing simulated produced water.

4. Conclusions

The effect of welding heat input on the corrosion resistance of A106B steel weld metal was evaluated by using the electrochemical tests. The number of acicular ferrite decreased and the number of irregular polygonal ferrite increased with welding heat input increasing. The electrochemical test results showed that weld metal with a large number of irregular polygonal ferrite performed higher corrosion resistance. The bottom center of specimens with different welding heat inputs was analyzed with electron backscatter diffraction (EBSD) technique. The results showed that the {101} crystal planes parallel to the surface could provide samples with high corrosion resistance, and the corrosion rate anisotropy was closely tied up with the surface energy anisotropy. Meanwhile, samples with a low dispersion degree of grain size showed high corrosion resistance, while the corrosion resistance of samples had nothing to do with grain boundary type.

Acknowledgments

The authors are grateful to the Natural Science Foundation of Tianjin, China (13JCYBJC18200), and the authors also wish to express their thanks to the Offshore Oil Engineering Co., Ltd., China for providing the A106B steel weld joint samples.

References

1. Z. Jia, X. Li, C. Du, Z. Liu, and J. Gao, Effect of the Carbon Dioxide Pressure on the Electrochemical Behavior of 3Cr Low Alloyed Steel at High Temperature, *Mater. Chem. Phys.*, 2012, **136**, p 973–979
2. Z. Cui, S. Wu, S. Zhu, and X. Yang, Study on Corrosion Properties of Pipelines in Simulated Produced Water Saturated with Supercritical CO_2, *Appl. Surf. Sci.*, 2006, **252**, p 2368–2374
3. Y. Zhang, X. Pang, S. Qu, X. Li, and K. Gao, Discussion of the CO_2 Corrosion Mechanism Between Low Partial Pressure and Supercritical Condition, *Corros. Sci.*, 2012, **59**, p 186–197
4. K. George and S. Nešic, Investigation of Carbon Dioxide Corrosion of Mild Steel in the Presence of Acetic Acid-Part 1: Basic Mechanisms, *Corrosion.*, 2007, **63**, p 178–186
5. L. Zhang, X. Li, C. Du, and Y. Cheng, Corrosion and Stress Corrosion Cracking Behavior of X70 Pipeline Steel in a CO_2-Containing Solution, *J. Mater. Eng. Perform.*, 2009, **18**, p 319–323
6. M. Kermani and A. Morshed, Carbon Dioxide Corrosion in Oil and Gas Production-A Compendium, *Corrosion.*, 2003, **59**, p 659–683
7. G. Zhang and Y. Cheng, On the Fundamentals of Electrochemical Corrosion of X65 Steel in CO_2-Containing Formation Water in the Presence of Acetic Acid in Petroleum Production, *Corros. Sci.*, 2009, **51**, p 87–94
8. F.F. Eliyan, E.-S. Mahdi, and A. Alfantazi, Electrochemical Evaluation of the Corrosion Behaviour of API-X100 Pipeline Steel in Aerated Bicarbonate Solutions, *Corros. Sci.*, 2012, **58**, p 181–191
9. J. Hernandez, A. Muñoz, and J. Genesca, Formation of Iron-Carbonate Scale-Layer and Corrosion Mechanism of API, X70 Pipeline Steel in Carbon Dioxide-Saturated 3% Sodium Chloride, *Afinidad*, 2012, **69**, p 251–258

10. S. Guo, L. Xu, L. Zhang, W. Chang, and M. Lu, Corrosion of Alloy Steels Containing 2% Chromium in CO_2 Environments, *Corros. Sci.*, 2012, **63**, p 246–258
11. C. Avendano-Castro, R. Galvan-Martinez, A. Contreras, M. Salazar, R. Orozco-Cruz, E. Martinez et al., Corrosion Kinetics of Pipeline Carbon Steel Weld Immersed in Aqueous Solution Containing H_2S, *Corros. Eng. Sci. Technol.*, 2009, **44**, p 149–156
12. M. Alizadeh and S. Bordbar, The Influence of Microstructure on the Protective Properties of the Corrosion Product Layer Generated on the Welded API, X70 Steel in Chloride Solution, *Corros. Sci.*, 2013, **70**, p 170–179
13. A.R. Shankar, G. Gopalakrishnan, V. Balusamy, and U.K. Mudali, Effect of Heat Input on Microstructural Changes and Corrosion Behavior of Commercially Pure Titanium Welds in Nitric Acid Medium, *J. Mater. Eng. Perform.*, 2009, **18**, p 1116–1123
14. Y. Han, H. Jing, and L. Xu, Welding Heat Input Effect on the Hydrogen Permeation in the X80 Steel Welded Joints, *Mater. Chem. Phys.*, 2012, **132**, p 216–222
15. C. Du, X. Li, P. Liang, Z. Liu, G. Jia, and Y. Cheng, Effects of Microstructure on Corrosion of X70 Pipe Steel in an Alkaline Soil, *J. Mater. Eng. Perform.*, 2009, **18**, p 216–220
16. K. Deen, R. Ahmad, I. Khan, and Z. Farahat, Microstructural Study and Electrochemical Behavior of Low Alloy Steel Weldment, *Mater. Des.*, 2010, **31**, p 3051–3055
17. H.-H. Huang, W.-T. Tsai, and J.-T. Lee, The Influences of Microstructure and Composition on the Electrochemical Behavior of A516 Steel Weldment, *Corros. Sci.*, 1994, **36**, p 1027–1038
18. G. Thewlis, Classification and Quantification of Microstructures in Steels, *Mater. Sci. Technol.*, 2004, **20**, p 143–160
19. J.S. Lee, S.H. Jeong, D.Y. Lim, J.O. Yun, and M.H. Kim, Effects of Welding Heat and Travel Speed on the Impact Property and Microstructure of FC Welds, *Met. Mater. Int.*, 2010, **16**, p 827–832
20. K.-T. Park, S.W. Hwang, J.H. Ji, and C.H. Lee, Inclusions Nucleating Intragranular Polygonal Ferrite and Acicular Ferrite in Low Alloyed Carbon Manganese Steel Welds, *Met. Mater. Int.*, 2011, **17**, p 349–356
21. L. Cui, X. Yang, D. Wang, X. Hou, J. Cao, and W. Xu, Friction Taper Plug Welding for S355 Steel in Underwater Wet Conditions: Welding Performance, Microstructures and Mechanical Properties, *Mater. Sci. Eng. A*, 2014, **611**, p 15–28
22. O. Grong and D.K. Matlock, Microstructural Development in Mild and Low-Alloy Steel Weld Metals, *Int. Met. Rev.*, 1986, **31**, p 27–48
23. G. Zhang and Y. Cheng, Micro-electrochemical Characterization of Corrosion of Welded X70 Pipeline Steel in Near-Neutral pH Solution, *Corros. Sci.*, 2009, **51**, p 1714–1724
24. H.R. Soleymani and M.E. Ismail, Comparing Corrosion Measurement Methods to Assess the Corrosion Activity of Laboratory OPC and HPC Concrete Specimens, *Cem. Concr. Res.*, 2004, **34**, p 2037–2044
25. H. Al-Mazeedi and R. Cottis, A Practical Evaluation of Electrochemical Noise Parameters as Indicators of Corrosion Type, *Electrochim. Acta*, 2004, **49**, p 2787–2793
26. M. Pourbaix, Applications of Electrochemistry in Corrosion Science and in Practice, *Corros. Sci.*, 1974, **14**, p 25–82
27. F. Farelas, M. Galicia, B. Brown, S. Nesic, and H. Castaneda, Evolution of Dissolution Processes at the Interface of Carbon Steel Corroding in a CO_2 Environment Studied by EIS, *Corros. Sci.*, 2010, **52**, p 509–517
28. S. Nešic and K.-L. Lee, A Mechanistic Model for Carbon Dioxide Corrosion of Mild Steel in the Presence of Protective Iron Carbonate Films-Part 3: Film Growth Model, *Corrosion*, 2003, **59**, p 616–628
29. J. Zhang, Z.L. Wang, Z.M. Wang, and X. Han, Chemical Analysis of the Initial Corrosion Layer on Pipeline Steels in Simulated CO_2-Enhanced Oil Recovery Brines, *Corros. Sci.*, 2012, **65**, p 397–404
30. M.S. Akram and V. Lomadze, On Some Basics of Linear Systems Theory, *Syst. Control Lett.*, 2009, **58**, p 83–90
31. M. Urquidi-Macdonald, S. Real, and D.D. Macdonald, Application of Kramers-Kronig Transforms in the Analysis of Electrochemical Impedance Data II. Transformations in the Complex Plane, *J. Electrochem. Soc.*, 1986, **133**, p 2018–2024
32. M. Urquidi-Macdonald, S. Real, and D.D. Macdonald, Applications of Kramers—Kronig Transforms in the Analysis of Electrochemical Impedance Data—III. Stability and Linearity, *Electrochim. Acta*, 1990, **35**, p 1559–1566
33. H. Shin and F. Mansfeld, Concerning the Use of the Kramers-Kronig Transforms for the Validation of Impedance Data, *Corros. Sci.*, 1988, **28**, p 933–938
34. Z. Feng, X. Cheng, C. Dong, L. Xu, and X. Li, Passivity of 316L Stainless Steel in Borate Buffer Solution Studied by Mott-Schottky Analysis, Atomic Absorption Spectrometry and X-ray Photoelectron Spectroscopy, *Corros. Sci.*, 2010, **52**, p 3646–3653
35. G. Zhang and Y. Cheng, Corrosion of X65 Steel in CO_2-Saturated Oilfield Formation Water in the Absence and Presence of Acetic Acid, *Corros. Sci.*, 2009, **51**, p 1589–1595
36. J. Sun, G. Zhang, W. Liu, and M. Lu, The Formation Mechanism of Corrosion Scale and Electrochemical Characteristic of Low Alloy Steel in Carbon Dioxide-Saturated Solution, *Corros. Sci.*, 2012, **57**, p 131–138
37. J.M. Bockris and D. Drazic, The Kinetics of Deposition and Dissolution of Iron: Effect of Alloying Impurities, *Electrochim. Acta*, 1962, **7**, p 293–313
38. S. Nešić, Key Issues Related to Modelling of Internal Corrosion of Oil and Gas Pipelines—A Review, *Corros. Sci.*, 2007, **49**, p 4308–4338
39. Wu K-h, Zhu L-q, Li W-p, and Liu H-c, Effect of Ca^{2+} and Mg^{2+} on Corrosion and Scaling of Galvanized Steel Pipe in Simulated Geothermal Water, *Corros. Sci.*, 2010, **52**, p 2244–2249
40. C.-N. Cao, On the Impedance Plane Displays for Irreversible Electrode Reactions Based on the Stability Conditions of the Steady-State—I. One State Variable Besides Electrode Potential, *Electrochim. Acta*, 1990, **35**, p 831–836
41. Y. Zhi-Ming and Y. Deng-Feng, A Theoretical Method to Calculate the Surface Free Energies of Crystals, *Acta Phys. Sin.*, 2005, **54**(8), p 3822–3830
42. L. Pauling, *The Nature of the Chemical Bond and the Structure of Molecules and Crystals: An Introduction to Modern Structural Chemistry*, Cornell University Press, Ithaca, 1960
43. J. Gray, B. El Dasher, and C. Orme, Competitive Effects of Metal Dissolution and Passivation Modulated by Surface Structure: An AFM and EBSD Study of the Corrosion of Alloy 22, *Surf. Sci.*, 2006, **600**, p 2488–2494
44. B.R. Kumar, R. Singh, B. Mahato, P. De, N. Bandyopadhyay, and D. Bhattacharya, Effect of Texture on Corrosion Behavior of AISI, 304L Stainless Steel, *Mater. Charact.*, 2005, **54**, p 141–147
45. H. Park and J. Szpunar, The Role of Texture and Morphology in Optimizing the Corrosion Resistance of Zinc-Based Electrogalvanized Coatings, *Corros. Sci.*, 1998, **40**, p 525–545
46. K. Ralston, N. Birbilis, and C. Davies, Revealing the Relationship Between Grain Size and Corrosion Rate of Metals, *Scripta Mater.*, 2010, **63**, p 1201–1204
47. Van Hunnik E, Pots B, Hendriksen E. The Formation of Protective $FeCO_3$ Corrosion Product Layers in CO_2 Corrosion, Paper No. 6. CORROSION/96, NACE International, Houston, TX, 1996
48. T. Minoda and H. Yoshida, Effect of Grain Boundary Characteristics on Intergranular Corrosion Resistance of 6061 Aluminum Alloy Extrusion, *Metall. Mater. Trans. A.*, 2002, **33**, p 2891–2898
49. H. Tanaka, H. Esaki, K. Yamada, K. Shibue, and H. Yoshida, Improvement of Mechanical Properties of 7475 Based Aluminum Alloy Sheets by Controlled Warm Rolling, *Mater. Trans.*, 2004, **45**, p 69–74